A novel method for the measurement of flotation recovery by means of 4D particle tracking velocimetry

A.-E. Sommer[a,*], M. Nikpay[a], S. Heitkam[b], K. Eckert[a,b]

[a] *Helmholtz-Zentrum Dresden-Rossendorf, Institute of Fluid Dynamics, 01314 Dresden, Germany*
[b] *Technical University Dresden, Institute of Process Engineering and Environmental Technology, 01062 Dresden, Germany*

Abstract

This work focuses on the analysis of flotation recovery through a simultaneous time-resolved measurement of particle and bubble trajectories. We introduced a new method that determined the probability of collision and attachment through a 3D particle tracking method with a high temporal (5 kHz) and spatial (16 pixels/mm) resolution in a dense particle flow (10000 particle/ml). A tomographic particle image velocimetry device with three high-speed cameras recorded the three-phase flow in a rectangular bubble column (bubble chain, 4 mm). Model particles with a fluorescent coating were employed so that particles appeared bright and bubbles dark on the captured images. An attachment occurred if the trajectory of a particle coincided with that of a bubble. The recovery was calculated based on the amount of particles attached to a bubble compared to the total particles density. We investigated its dependency on different model particles (polystyrene, polymethyl methacrylate) and particle diameter (10-100 μm).

Keywords: Collection zone recovery, Particle tracking velocimetry, PMMA flotation

1. Introduction

Froth flotation is the most important and widely used process for the separation of minerals. The success of any flotation process depends heavily on an efficient interaction of suitably hydrophobized particles and bubbles in the pulp and is therefore controlled by both the surface chemistry and the hydrodynamics in the pulp. The performance of flotation is quantified in terms of the recovery as a measure of the number of target particles at various times in a reference volume. The rate of removal of the target particles in batchwise flotation may be described frequently by a first order rate equation with a kinetic constant k. Ultimate goal is to predict the flotation rate constants for minerals from first principles (e.g. Sutherland (1948); Ralston et al. (1999); Yoon (2000); Nguyen and Schulze (2003))

For that purpose the particle capture process in the pulp is divided in a sequence of elementary subprocess, namely collision, attachment and detachment, which are represented by probabilities P_i. These probabilities are modeled in terms of physico-chemical and geometrical parameters (e.g. Sharma and Ruckenstein (1990); YOON and LUTTRELL (1989)), such as contact angle or bubble-to-particle radius, and the Reynolds number of bubbles Schubert (1999)

Thus, a direct way to measure recovery at defined hydrodynamic conditions would be very helpful to verify these models and to advance our understanding of particular microprocesses. To do so, this work presents a new approach to measure the collection zone recovery. It is based on optical 4D particle tracking velocimetry (PTV) which is used to identify attached particles on bubbles. In contrast to other methods, based e.g. on a sampling tube inserted below the pulp interface to collect loaded bubbles (Seaman et al. (2004)), this method is completely non-invasive. While the former 3D PTV was restricted to a low particle

*Corresponding author
Email address: a.sommer@hzdr.de (A.-E. Sommer)

seeding density (0.005 particles per pixel (Schanz et al. (2016))) recent developments in this field enable the application of PTV with a much higher particle densities as predominated in the pulp zone of a flotation cell. Milestones are a time resolved tomographic particle image velocimetry (tomo PIV) (Scarano (2013)) and advanced tracking algorithms as the Shake-the-box algorithm from Schanz et al. (2016).

Based on the recorded images, we develop a method to identify attached particles. A bubble mask is generated to separate the bubble and particle image. The tracks for each phase are calculated individually with the algorithm of Schanz et al. (2016) and Maas (1996). The attached particles are located through their relative position to the bubble surface and their slip velocity. Finally, the collection zone recovery is calculated as a ratio of attached particles to all particles in the system boundaries.

2. Experimental facility

2.1. Bubble column

To generate a simple model flow in order to prove the method, the experiments were carried out in a rectangular bubble column with an inner size of 90×25 mm^2 and a water level of 200 mm as shown in Fig. 1. The particle and bubble trajectories were measured 60 mm above the ground plate in the volume $100 \times 50 \times 10$ mm^3 along the center. A bubble chain was introduced by a needle with an inner diameter of 0.3 mm. The outlet for the pressurized air as gaseous phase was 65 mm above the ground plate. The volume flow was measured and controlled by a mass flow controller. The used volume flow rate was 0.01 l/min. This setup allowed us to produce bubbles with a reproducible position and movement. Regarding the experiments from Ziegenhein (2016) a bubble size of 3 mm was expected.

2.2. Flotation chemistry

The attachment of Polymethyl methacrylate (PMMA) particles to a bubble is influenced by their contact angle and wetting behavior. To favor this process, we introduced a novel solution for surface modification by using two different surfactants. Initially, the nonionic surfactant solution was used as an antistatic agent to treat the PMMA surfaces. Afterward, by adding cationic surfactant the polymer surface was charged over night. The first chemical solution was prepared using 3.75 g/l IGEPAL CO-890 nonionic surfactant and concentration above its critical micelle concentration (CMC) of 0.5946 g/l. The second solution is cetyltrimethylammonium bromide (CTAB) with a concentration of 0.3 g/l which is lower than its CMC (0.364 g/l). Deionized water is used for the preparation of solutions. The chemicals were supplied by Sigma-Aldrich Chemicals Co. 40 ml of this mixture was applied to 1 ml PMMA particles (30% w/v). For the experiments, the desired amount of particles within the solution (10 ml) was added to the bubble column filled with deionized water.

3. 4D Particle tracking velocimetry

3.1. Measurement device

For the PTV measurement, we used a tomo PIV system (Fig. 1) supplied by LaVision. Tomo PIV is an optical 3D measurement technique for the velocity of tracer particles. Tracer particles in the measurement volume are illuminated by a laser. The scattered light from these particles is captured with at least three cameras from different viewing angles. In traditional tomo PIV, this set of recorded images is used for the tomographic reconstruction and subsquent cross correlation between the reconstructed volumes. The result is a 3D,3C velocity field of the investigated flow. A more detailed review of this measurement technique is given by Scarano (2013). In contrast, PTV triangulates the position of each particle at each time step. The results characterize the velocity field of the liquid phase or the Lagrangian particle trajectories.

For our application, we adopted this technique as followed (Tab. 1). Three high-speed cameras in a linear imaging configuration observed the measurement volume. We used fluorescent PMMA Rhodomain B particles (particle diameter $d_p = 50$ - 100 μm) which were illuminated by a Nd-YLF laser ($\lambda = 527$ nm). The fluorescent Rhodamin B dye caused the absorption of the laser light and emitted the light with a wavelength λ_{em} of 584 nm.

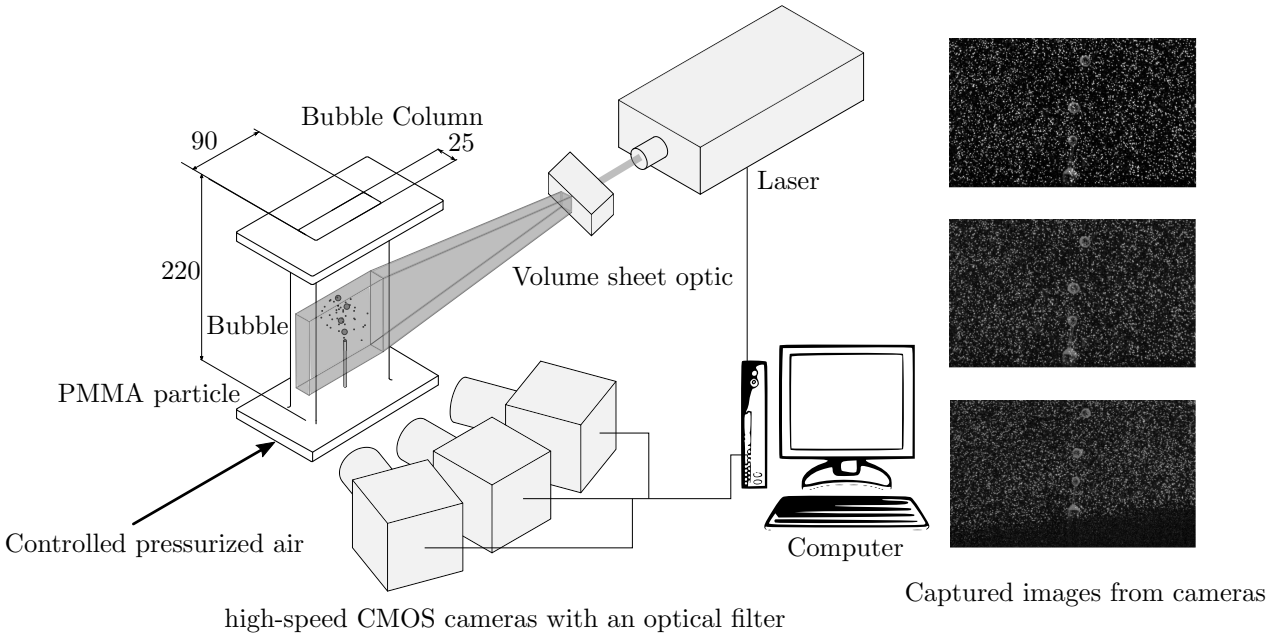


Figure 1: Experimental setup of the tomo PIV system to measure the particle attachment in a bubble column.

Fluorescent particles as seeding particles were used for bubbly two-phase flows by various research groups (e.g. Lindken and Merzkirch (2002), Ziegenhein and Lucas (2016)). An optical long pass filter was applied to the cameras to only record light emitted by the fluorescent seeding particles. The scattered laser light from the bubbles was blocked. But the bubbles also reflected the fluorescent light. This enabled a simultaneous recording of bubbles and particles. The separation of these two signals is described in detail in the following section.

Before each measurement a spatial calibration was carried out. For a success particle triangulation of the Shake-the-Box algorithm, a calibration error lower than a fraction of the particle image diameter (Elsinga et al. (2006)) was required. Therefore, the mapping function was not only calculated through an image of a two plane calibration plate (50 mm x 50 mm) but also the volume self-calibration procedure from Wieneke (2008) was applied. A set of images with a lower seeding density and no air bubbles were recorded. The 3D position of each particle was computed by triangulation of matching particles. The residual triangulation error was then used to correct the mapping functions for all cameras. This procedure detected large misalignment errors (up to several pixels) and reduced them to below 0.1 px in the entire measurement volume which was necessary for successful triangulation in the Shake-the-box algorithm.

3.2. Image processing

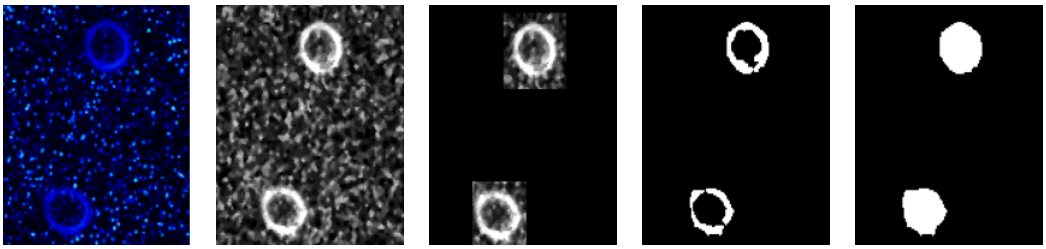
For the calculation of the collection zone recovery R_c the data analysis of the recorded image was divided into two subprocess. First, the bubble and particle trajectories were computed. Hereby, an image processing algorithm was applied to compute a bubble mask. Second, the attached particles were detected in order to calculate R_c. This part is described in the next section.

The image processing algorithm for masking out the bubbles was inspired by Lindken and Merzkirch (2002). The particles in the image were removed by a 3×3 px median filter (Fig. 2b). In the next step, a circular Hough transformation (Atherton and Kerbyson (1999), Yuen et al. (1989)) was used to recognize the 2D bubble image as a circular object (Fig. 2c). The detected bubbles were cut out and segmented individually. This was possible because the bubbles in the bubble chain remained well separately.

For the binarization, an adaptive gray value threshold was applied (Fig. 2d). The bubble in the image is a bright circular ring and a dark circle in the middle as seen in Fig. 3a. The corresponding gray values along the middle axis of the bubble are illustrated in Fig. 3b. Therefore, the boundaries of the bubble were

Seeding	Material	PMMA - Rhodamin B
	Diameter	$50 - 100$ μm
	Density	1.188 g/cm^3
	Concentration	0.65 particles/mm^3
Illumination	Intensity	31 W
	λ	527 nm
	Measurement volume thickness	10 mm
Recording	Resolution	1280 px x 800 px
	Frame rate	1000 fps
	Exposure time	1000 μs
	Field of view	80 mm x 50 mm
	Image depth	8 Bit

Table 1: Properties and parameters of tomo PIV setup.



(a) (b) (c) (d) (e)

Figure 2: Image processing steps to define a mask for bubbles in the captured images. (a) Original image. (b) Image preprocessing to remove particles with a median filter. (c) Cropped bubble image after Hough transformation. (d) Binarization with adaptive gray value threshold. (e) Image of bubble mask after filling up non-detected bubble areas.

defined by the highest gradient before or respectively after the highest gray value in Fig. 3b. The applied threshold for the binarization was the mean gray value between the boundaries of the bubble. Finally, the non-detected bubble areas were filled up yielding the bubble mask (Fig. 2e).

3.3. Trajectory calculation

In the next step, the trajectories were calculated for each phase separately. The particle trajectories were triangulated with the Shake-the-box algorithm supplied by LaVision's software DaVis 8.4. This algorithm computed the Lagrangian tracks of particles through triangulation with an extensive use of their temporal information. A more detailed description of this algorithm can be found in Schanz et al. (2016). The Shake-the-box algorithm was applied to the captured tomo PIV images. To avoid errors caused by the recorded bubbles in these images, the bubble areas were subtracted by the intensity value of the bubble (Fig. 4a). Consequently, particles located in front of the bubble remained in the image, if their image intensity was higher than the one from the bubble. The results of this algorithm are illustrated for ten time steps in Fig. 4b.

Simultaneously, the bubble trajectories were determined using a 3D PTV algorithm from Maas et al. (1993) in LaVision's software DaVis 8.4. The lower number of tracked object allowed the application of a general and less computation time-consuming algorithm. The PTV algorithm from Maas et al. (1993) was applied to the midpoints of the bubble (Fig. 4c).

Both algorithm provided results in form of a trajectory. The trajectory consists of the respective position X_j which is a tuple of the three coordinates (x_j, y_j, z_j) and its velocity vector $\boldsymbol{V_j}$ with its three velocity component in each direction in space (u_j, v_j, w_j). For further explanations the following notation is used

- Points: capital letters e.g. X_b, X_p

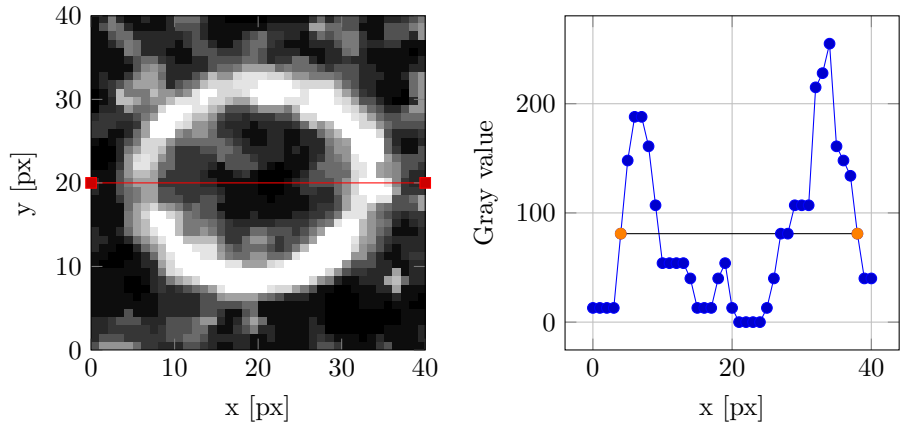


Figure 3: Calculation adaptive gray value threshold. (a) Appearance of the bubble in the image with a bright circular ring and a dark circle in the middle. (b) Corresponding gray values along the middle axis of a bubble (illustrated as red line in (a)). The threshold value is illustrated as orange points.

- Vectors: capital letters in bold e.g. $\boldsymbol{V_b}$, $\boldsymbol{V_p}$
- Coordinates, velocity components for each direction in space: small letters e.g. x_b, u_p.

Thereof, the particle and bubble trajectories are described with these variables

$$\text{Particle}: X_p(x_p, y_p, z_p),\ \boldsymbol{V_p}(u_p, v_p, w_p)$$
$$\text{Bubble}: X_b(x_b, y_b, z_b),\ \boldsymbol{V_b}(u_b, v_b, w_b)$$

To quantify the interaction between particles and bubbles, the shape of each object was approximated and their trajectories were combined again. Particles were described as points whereas the bubble shape was approximated as an oblate spheroid (Fig. 5). This approximation bases on Grace's bubble shape prediction diagramm (Clift et al. (2005)) taking the Eötvös Eo and Morton number Mo into account

$$Eo = \frac{\rho_l g d_b^2}{\sigma} = 1.65 \tag{1}$$
$$Mo = \frac{g \upsilon_l^4 \Delta\rho}{\rho_l^2 \sigma^3} = 7 \cdot 10^{-11} \tag{2}$$

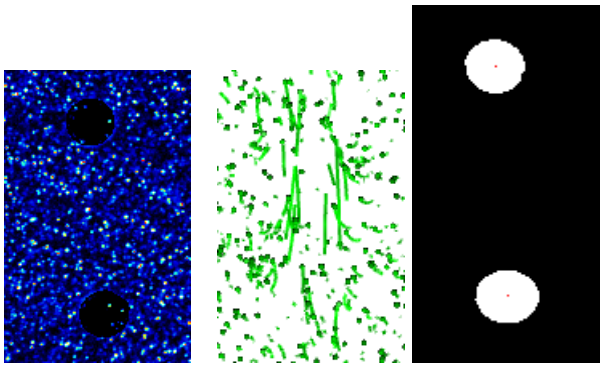
with ρ_l the liquid density, g the gravitational constant, d_b the volume equivilant bubble diameter, σ the surface tension, $\Delta\rho$ the density difference between gas and liquid phase and υ_l the liquid kinematic viscosity. Clift et al. (2005) predicted spherical and ellipsoidal bubble shapes in this range.

The algebraic equation (Zwillinger (2002)) of an oblate spheroid is

$$\frac{x^2 + z^2}{a^2} + \frac{y^2}{c^2} = 1. \tag{3}$$

The inclination angle α, major semi-axis a and minor semi-axis c from each bubble were extracted from the 2D image of the bubble. Unfortunately, the general assumption for Eq. (3) is that the spheroid is not rotated and the midpoint equals the origin of the coordinate system. These assumptions did not apply for rising bubbles. Through the movement of the bubble, a translation of the midpoint and a rotation of the semi-axis occurred in every time step. Consequently, a transformation of the coordinate system was necessary to fulfill the criteria for Eq. (3).

The coordinate system was translated to the midpoint of the bubble X_b and rotated around the bubble's angle of inclination in the xy-plane to receive the coordinate system of the bubble(Fig. 6). This led to the



(a) (b) (c)

Figure 4: Image processing steps to calculate particle (a,b) and bubble trajectory(c). (a) Subtraction of bubble mask from original image. (b) Calculated particle trajectories with Shake-the-box algorithm for ten time steps. (c) Extracted bubble mask where the mid points are highlighted red.

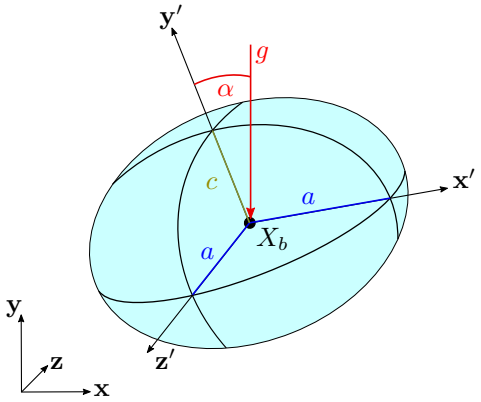


Figure 5: Definition of rotated spheroid with $a > c$ the semi-axis, X_b the mid point and inclination angle α between axis of symmetry and gravitation g. The illustration is within the global (x, y, z) and transformed (x', y', z') coordinate system.

following transformation

$$X' = \begin{bmatrix} \cos(\alpha) & -\sin(\alpha) & 0 \\ \sin(\alpha) & \cos(\alpha) & 0 \\ 0 & 0 & 1 \end{bmatrix} \cdot X - X_b \tag{4}$$

Consequently, in the transformed coordinate system Eq. (3) was used for further calculations. In the following sections all vectors are defined within the coordinate system of the bubble. For the sake of simplicity, we suppress the prime in the following sections. Hence, there is no distinction to the global coordinate system.

3.4. Calculation of collection zone recovery based on the number of attached particles

Collection zone recovery R_c is defined in this work as

$$R_c = \frac{N_{att}}{N_{all}} \cdot 100\% \tag{5}$$

where N_{all} refers to the number of all particles within the system boundary, see Fig. 6. Hereby, the significance was to determine N_{att}. We set up the following conditions to identify attached particles. These criteria were based on the last measured point of the particle trajectory.

(i) The particle is situated inside the system boundaries of the bubble.

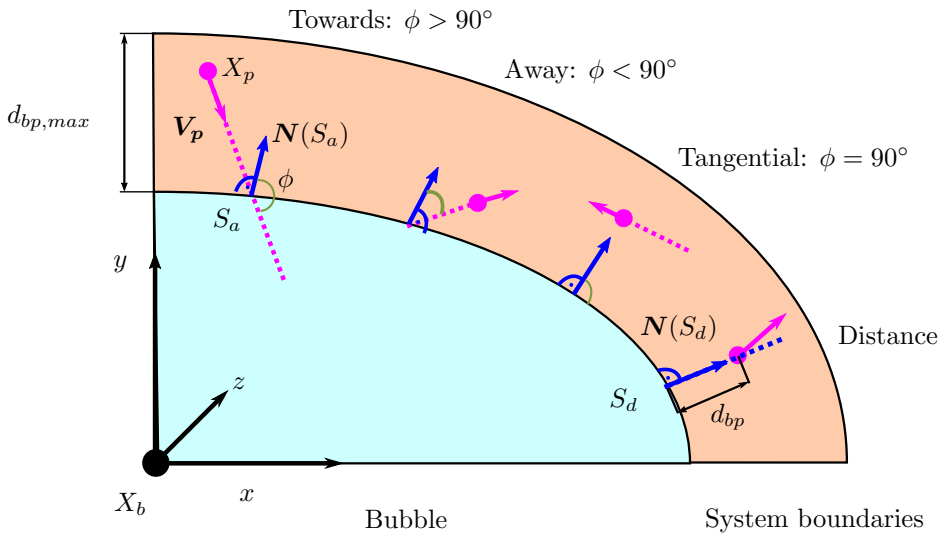


Figure 6: Definition of system boundaries with $d_{bp,max}$ as distance particle to bubble surface and vectors of bubble surface and particle to localize their movement in reference to each other.

(ii) The particle moves towards the bubble.

(iii) The slip velocity $\boldsymbol{V_s}$ between bubble $\boldsymbol{V_b}$ and particle velocity $\boldsymbol{V_p}$ is below the threshold $\boldsymbol{V_{s,max}}$

$$\boldsymbol{V_s} = \boldsymbol{V_b} - \boldsymbol{V_p} < \boldsymbol{V_{s,max}}. \tag{6}$$

(iv) The particle trajectory should contain at least three track points.

We defined the system boundary to be a thin layer outside the bubble surface. All particles within a maximum distance to the bubble surface of $d_{bp,max}$ were localized inside, the others outside the system boundary as illustrated in Fig. 6. For the evaluation of the criterion (i), the distance d_{bp} between particle X_p and bubble surface S was computed.

The problem was to find the point S_d on the bubble surface which had the minimum distance to X_p. The minimum distance was orthogonal to the bubble surface. Therefore, the perpendicular normal vector $\boldsymbol{N}$ on a given point on the surface S was used. The desired normal vector $\boldsymbol{N}(S_d)$ had to point towards X_p.

$$X_p = S_d + d_{bp} \cdot \boldsymbol{N}(S_d) \tag{7}$$

The normal vector $\boldsymbol{N}(S)$ is defined as the gradient of the surface on the point S with its coordinates (s_x, s_y, s_z)

$$\boldsymbol{N} = \frac{1}{|\boldsymbol{N}|}\nabla\left(\frac{s_x^2 + s_z^2}{a^2} + \frac{s_y^2}{c^2}\right) = \begin{bmatrix} \frac{2 \cdot s_x}{a^2} \\ \frac{2 \cdot s_y}{c^2} \\ \frac{2 \cdot s_z}{a^2} \end{bmatrix}. \tag{8}$$

To solve Eq. (7) and gain d_{bp}, another equation was required as this equation contained four unknown variables (s_{dx}, s_{dy}, s_{dz}, d_{bp}). Therefore, Eq. (3) was used because S_d has to stay on the surface of the spheroid. After solving this equation system, the minimum distance d_{bp} between S_d and X_p was found.

Criterion (ii) compares the direction of the movement between particle and bubble. In Fig. 6 the three possible cases are illustrated. The particle can move towards the bubble, away from the bubble or tangential to the bubble surface. To decide which case applied for a certain particle, the angle ϕ in point S_a between particle velocity ($\boldsymbol{V_p}$) and normal vector $\boldsymbol{N}(S_a)$ was computed. Hereby, the normal vector was located on the intersection point S_a between particle trajectory and bubble surface.

To find S_a, the same procedure was applied as described before to localize S_d. But instead of Eq. (7), the equation of the particle trajectory was used

$$S_a = X_p + t \cdot \boldsymbol{V_p} \tag{9}$$

Angle ϕ [°]	Classification of particle flow
< 90	Away from bubble surface.
$= 90$	Tangential along bubble surface.
> 90	Towards bubble surface.

Table 2: Classification of particles according their movement direction in reference to the bubble surface.

Parameter	Deionized water Ziegenhein (2016)	Deionized water with surfactants
d_b [mm]	3.5	2
Eo	1.65	0.75
Mo	$2.63 \cdot 10^{-11}$	$7 \cdot 10^{-11}$

Table 3: Bubble properties compared the study study from Ziegenhein (2016) in deionized water to our study with added surfactants (IGEPAL CO-890 and CTAB) to the deionized water. Volume flow rate = 0.01 l/min

with t the time a particle needs to move from position X_p to S_a.

The angle ϕ between $\boldsymbol{V_p}$ and $\boldsymbol{N}(S_a)$ was defined as

$$\cos\phi = \frac{\boldsymbol{V_p} \cdot \boldsymbol{N}(S_a)}{|\boldsymbol{V_p}| \cdot |\boldsymbol{N}(S_a)|}. \tag{10}$$

As seen in Fig. 6, ϕ is the smallest angle between both vectors. The classification is listed in Tab. 2. Consequently, only particle trajectories with an angle higher than 90° were candidates for an attached particle.

Criteria (iii) and (iv) were proved directly with the results of the PTV. Finally, if a particle fulfilled all four criteria, it was classified as attached. The sum of these particles is N_{att}. All particles which add least accomplished criterion (i) were classified as particle in the system boundary. This sum is N_{all} and includes N_{att}. Based on these two values, the collection zone recovery was computed with Eq. (5).

4. Results

4.1. Characterization of flotation cell

In order to observe an attachment of a particle to a bubble, initial studies were made to prove the floatability of PMMA particles in our current setup. Many research groups focused on the flotation of PMMA and developed different strategies (Buchan and Yarar (1995); Fraunholcz (1997); Wang et al. (2017)). Most of them used organic liquids and other toxic substances why we developed an alternative method without toxic substance. For the flotation test, we increased the volume flow rate up to 0.5 l/min. After a one minute, the pink PMMA particles were observed on the froth (Fig. 7). This test revealed the floatability of PMMA particles with our novel method.

The added surfactants not only changed the wetting properties of the particles but also the surface tension σ of the liquid phase (Tab. 3). The surface tension of water ($T = 20°$) is 72.75 mN/m (Vargaftik et al. (1983)) whereas the surface tension within our setup was 51.9 mN/m. A decrease of the surface tension influenced the hydrodynamics within the flotation cell. The bubble diameter was smaller because of earlier bubble release at the nozzle due to the lower surfaces forces. Furthermore, surfactants enriched on the bubble surface which led to a rigid interface. These effects result in a change of Eo number (Tab. 3) which characterizes the bubble shape.

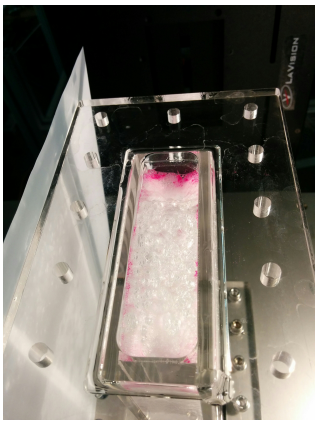


Figure 7: Image to proof the flotability pf pink PMMA particles.

4.2. Visualization of turbulence

Turbulence plays an important role in the flotation process. It affects the transport of solids, gas dispersion, particle-bubble collision, attachment and detachment. Thus, it has an impact on the recovery. Therefore, the measurement of the macroscopic flow and the microscopic turbulence within a flotation cell gives important information concerning the recovery rate.

If the particles follow the flow, PTV cannot only measure the recovery but also the flow field. One example is shown in Fig. 8. This figure illustrates the particle trajectories in the xy plane at $z = 0$ mm and zy plane at $x = 0$ mm during 20 time steps. The gas outlet is at position $(0, 0, 0)$. The particle trajectories are divided into three groups based on their velocity in y-direction v_p.

The first group includes all trajectories below 0.02 m/s. They are situated mainly at more than 5 mm from the center line. Closer to center line ($|x| < 5$ mm, $|z| < 2$ mm) the particle velocity increases. This rise can be divided into two parts based on their y position. In the part below $y = 25$ mm the majority of particles have a velocity above 0.15 m/s whereas in the higher part the most particles are in the range between 0.02 m/s and 0.15 m/s.

Due to the bubble wake, the particles have a higher velocity in the near field of the bubbly flow. This movement becomes weaker with a higher distance to the bubble ($|x| > 0.5$ mm, $|z| > 0.5$ mm). The sudden change of the particle velocity within the bubbly flow could be caused by the bubble path. The initial straight bubble path changed to a small zig-zag motion. This leads to a smaller rising velocity and a wider influence area. Therefore, 25 mm above the bubble outlet the particle velocity decreases but extends its area.

4.3. Particles in the system boundaries

The recovery is a quantification of the interaction between particle and bubble. Fig. 9 shows the particle trajectories in the system boundaries ($d_{bp,max} = \frac{a}{2}$) of one bubble accumulated over 250 time steps. The bubble shape was averaged over time. The particles were divided into two groups which are the attached and not attached particles. This diagram shows that the majority of particles are attached to the trailing edge of the bubble. This could be caused by the bubble introduced turbulence within the bubble wake.

Furthermore, Fig. 9 indicates that only a small number of particles are within the system boundaries. This situation is illustrated in more detail in Fig. 10 with the dependency between the average number of particles N_{all} and their distance to the bubble outlet. The particle number was averaged over all bubbles within the range of 7 mm and led to non-integer numbers for the amount of particles. N_{all} decreases with y.

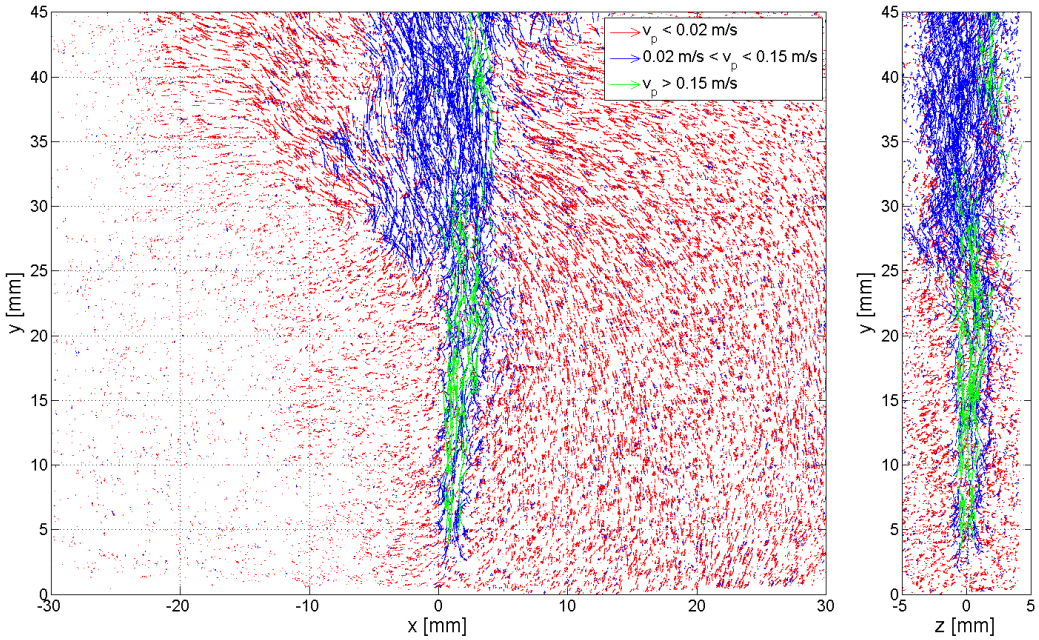


Figure 8: Particle trajectories of the measurement volume over 20 time steps. Left: xy plane at $z = 0$ mm. Right: zy plane at $x = 0$ mm. The color of each vector is based on its velocity in y-direction v_p.

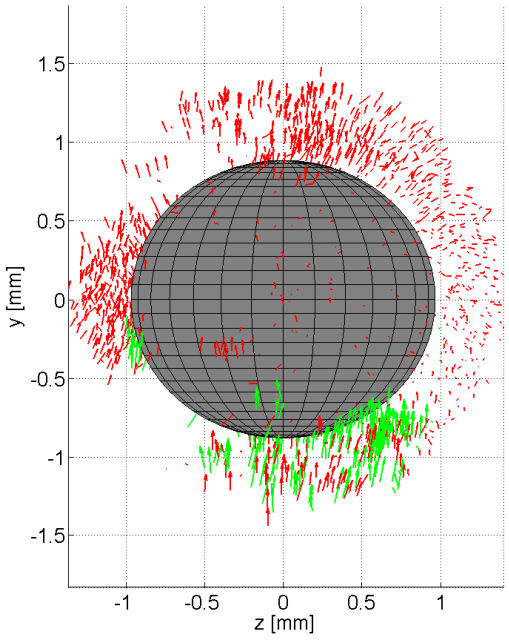


Figure 9: Particle trajectories with system boundaries of bubble over 250 time steps. The particle trajectory is colored green, if particle attached to bubble and red, if no attachment occurred. $N_{att} = 252$, $N_{all} = 1273$.

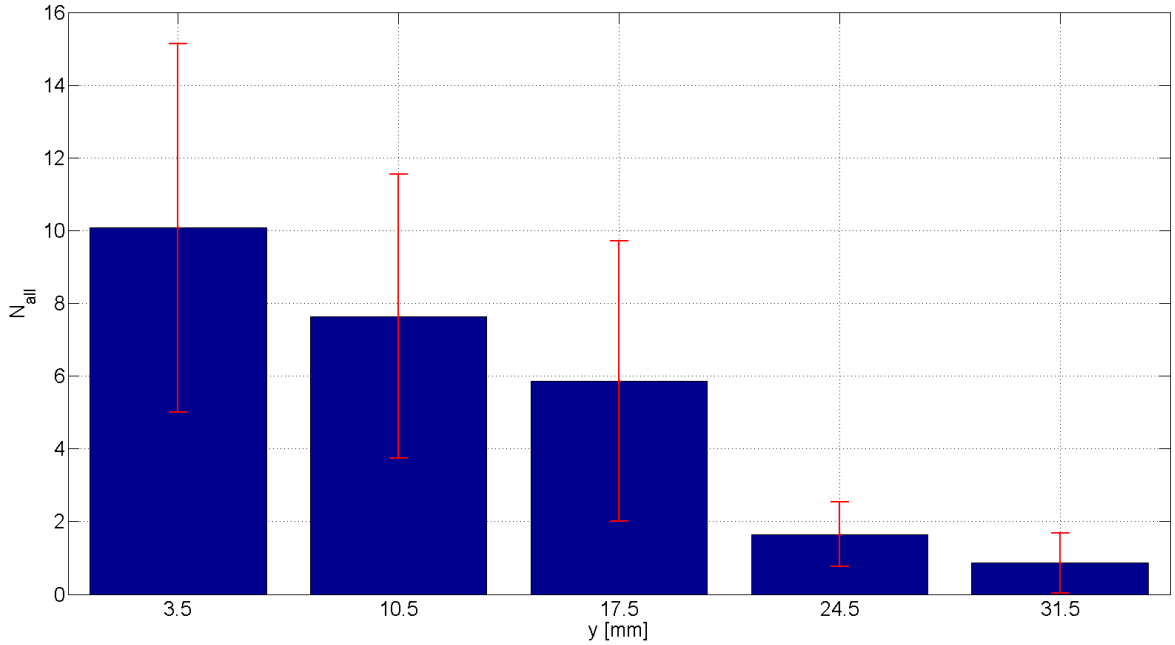


Figure 10: Dependency of averaged number of all particles within system boundary to the y-position range of the bubble. $d_{bp_max} = \frac{a}{2} = 0.5$ mm.

5. Discussion

Our presented method is a modification of PTV. Instead of applying tracer particles to measure the liquid flow, we used them as flotation particles. In our first application of this technique, we utilized PMMA tracer particles. The surface is easy to modify in form of a fluorescent coating, has a defined shape and a similar density to water. Although their neutral buoyancy in water is not comparable with other ores in flotation. These PMMA particles are more likely to follow the flow and sediment slowly because of their low-density difference to water. They can be used in the field of plastic flotation. In the field of mineral flotation, a fluorescent coating method for ores has to be developed to detect them with PTV. The advantage on the chosen particles is, that they are also applicable to measure the liquid flow because the slip velocity between liquid and particle is small. Therefore, the unsteady flow could be measured within Fig. 8.

We applied PTV in the macroscopic flow and near field of the bubble. In both cases, the Lagrangian particle trajectories were measured with a high temporal (1000 Hz) and spatial resolution (0.06 mm/px). Unfortunately, a trajectory of an attached particle on the bubble surface for multiple time steps has not been observed yet. After an attachment of a particle to the bubble surface, the fluorescent illumination of the bubble outshines the particle. Consequently, the particle is not detectable anymore. The same occurs if the particle moves behind the bubble and out of sign from the cameras. This effect is reflected in Fig. 10. Normally in a well mixed flotation cell, the number of particles in the system boundary is invariant to the height. Further experiments are required to resolve this issue.

Based on the low number of particles within the system boundaries the recovery rate was not calculated. Reasons regarding the experimental setup were a low seeding density and not efficient laser illumination. They will be improved through an optimized experimental setup in ongoing works.

Another technique to measure the Lagrangian particle trajectories in the 3D space is the Positron Emission Particle Tracking (PEPT) (Parker et al. (1993)). The main advantage of this method is the measurement in opaque flows but with a lower number of seeding particles (Barigou (2004), Langford et al. (2016)) and lower temporal and spatial resolution (Barigou (2004)). Also, PEPT requires a special treatment for the tracer particle. They have to be radioactive active. Therefore, PTV is more suitable to measure micro

turbulence and quantify its influence on interactions between particles and bubble. In contrast, PEPT can be used for the macroscopic flow measurements in a flotation cell with higher gas flow rates.

References

Atherton, T.J., Kerbyson, D.J., 1999. Size invariant circle detection. Image and Vision computing 17, 795–803.

Barigou, M., 2004. Particle tracking in opaque mixing systems: An overview of the capabilities of PET and PEPT. Chemical Engineering Research and Design 82, 1258–1267.

Buchan, R., Yarar, B., 1995. Recovering plastics for recycling by mineral processing techniques. JOM 47, 52–55. doi:10.1007/BF03221410.

Clift, R., Grace, J.R., Weber, M.E., 2005. Bubbles, Drops, and Particles. Courier Corporation.

Elsinga, G.E., Scarano, F., Wieneke, B., van Oudheusden, B.W., 2006. Tomographic particle image velocimetry. Experiments in Fluids 41, 933–947. doi:10.1007/s00348-006-0212-z.

Fraunholcz, N., 1997. Plastics flotation .

Langford, S., Wiggins, C., Tenpenny, D., Ruggles, A., 2016. Positron Emission Particle Tracking (PEPT) for Fluid Flow Measurements. Nuclear Engineering and Design 302, 81–89. doi:10.1016/j.nucengdes.2016.01.017.

Lindken, R., Merzkirch, W., 2002. A novel PIV technique for measurements in multiphase flows and its application to two-phase bubbly flows. Experiments in Fluids 33, 814–825. doi:10.1007/s00348-002-0500-1.

Maas, H.G., 1996. Contributions of Digital Photogrammetry to 3-D PTV, in: Three-Dimensional Velocity and Vorticity Measuring and Image Analysis Techniques. Springer, Dordrecht. ERCOFTAC Series, pp. 191–207. doi:10.1007/978-94-015-8727-3_9.

Maas, H.G., Gruen, A., Papantoniou, D., 1993. Particle tracking velocimetry in three-dimensional flows: Part 1. Photogrammetric determination of particle coordinates. Experiments in Fluids 15, 133–146. doi:10.1007/BF00190953.

Nguyen, A., Schulze, H.J., 2003. Colloidal science of flotation. volume 118. CRC Press.

Parker, D.J., Broadbent, C.J., Fowles, P., Hawkesworth, M.R., McNeil, P., 1993. Positron emission particle tracking-a technique for studying flow within engineering equipment. Nuclear Instruments and Methods in Physics Research Section A: Accelerators, Spectrometers, Detectors and Associated Equipment 326, 592–607.

Ralston, J., Fornasiero, D., Hayes, R., 1999. Bubbleparticle attachment and detachment in flotation. International Journal of Mineral Processing 56, 133 – 164. URL: http://www.sciencedirect.com/science/article/pii/S0301751698000465, doi:http://dx.doi.org/10.1016/S0301-7516(98)00046-5.

Scarano, F., 2013. Tomographic PIV: Principles and practice. Measurement Science and Technology 24, 012001. doi:10.1088/0957-0233/24/1/012001.

Schanz, D., Gesemann, S., Schröder, A., 2016. Shake-The-Box: Lagrangian particle tracking at high particle image densities. Experiments in Fluids 57, 70. doi:10.1007/s00348-016-2157-1.

Schubert, H., 1999. On the turbulence-controlled microprocesses in flotation machines. International Journal of Mineral Processing 56, 257 – 276. URL: http://www.sciencedirect.com/science/article/pii/S0301751698000489, doi:http://dx.doi.org/10.1016/S0301-7516(98)00048-9.

Seaman, D.R., Franzidis, J.P., Manlapig, E.V., 2004. Bubble load measurement in the pulp zone of industrial flotation machines - a new device for determining the froth recovery of attached particles. International Journal of Mineral Processing 74, 1–13. doi:10.1016/j.minpro.2004.04.001. wOS:000224927600001.

Sharma, A., Ruckenstein, E., 1990. Energetic criteria for the breakup of liquid films on nonwetting solid surfaces. Journal of Colloid and Interface Science 137, 433–445.

Sutherland, K., 1948. Physical chemistry of flotation. xi. kinetics of the flotation process. The Journal of Physical Chemistry 52, 394–425.

Vargaftik, N.B., Volkov, B., Voljak, L., 1983. International Tables of the Surface Tension of Water. https://www.researchgate.net/publication/258071214_International_Tables_of_the_Surface_Tension_of_Water. doi:http://dx.doi.org/10.1063/1.555688.

Wang, C.Q., Wang, H., Huang, L.L., 2017. A novel process for separation of polycarbonate, polyvinyl chloride and polymethyl methacrylate waste plastics by froth flotation. Waste Management (New York, N.Y.) 65, 3–10. doi:10.1016/j.wasman.2017.04.006.

Wieneke, B., 2008. Volume self-calibration for 3D particle image velocimetry. Experiments in Fluids 45, 549–556. doi:10.1007/s00348-008-0521-5.

Yoon, R.H., 2000. The role of hydrodynamic and surface forces in bubbleparticle interaction. International Journal of Mineral Processing 58, 129 – 143. URL: http://www.sciencedirect.com/science/article/pii/S030175169900071X, doi:http://dx.doi.org/10.1016/S0301-7516(99)00071-X.

YOON, R.H., LUTTRELL, G.H., 1989. The effect of bubble size on fine particle flotation. Mineral Processing and Extractive Metallurgy Review 5, 101–122.

Yuen, H.K., Princen, J., Dlingworth, J., Kittler, J., 1989. A Comparative Study of Hough Transform Methods for Circle Finding, Alvey Vision Club. pp. 29.1–29.6. doi:10.5244/C.3.29.

Ziegenhein, T., 2016. Fluid Dynamics of Bubbly Flows. Phd. Technische Universität Berlin.

Ziegenhein, T., Lucas, D., 2016. On sampling bias in multiphase flows: Particle image velocimetry in bubbly flows. Flow Measurement and Instrumentation 48, 36–41. doi:10.1016/j.flowmeasinst.2016.02.003.

Zwillinger, D., 2002. CRC Standard Mathematical Tables and Formulae. CRC press.